Ultrafast Dynamic Compression of Cyclohexane

Ashutosh Mohan[1,2,*], Ajay K. Mishra[1,2,+], S. Chaurasia[3,#], John Pasley[4], K. C. Gupta[1], T. Sakuntala[1,2]

[1]*High Pressure and Synchrotron Radiation Physics Division, Bhabha Atomic Research Centre, Mumbai-400085, India*
[2]*Homi Bhabha National Institute, Mumbai-400094, India*
[3]*School of Physics and Mathematics, Queen's University Belfast, BT7 1NN, U.K.*
[4]*York Plasma Institute, School of Physics, Engineering and Technology, University of York, York, YO10 5DD, U.K.*
Corresponding author: *ashutoshm@barc.gov.in; +akmishra@barc.gov.in; #s.chaurasia@qub.ac.uk

Abstract:

Cyclohexane, a key saturated cyclic hydrocarbon in petroleum, is a prospective molecular framework for energetic materials, making its phase diagram a subject of critical interest. Our work pushes the boundaries by exploring phase transitions under ultrafast (nanosecond timescale) dynamic compression using laser-driven shock and *in-situ* time-resolved Raman spectroscopy in contrast to previous study [C. Yuan, J. Wang, X. Zhang, Y. Xu, S. Feng, and H. Li, *J. Mol. Liq.* **363**, 119836 (2022)] reporting novel phases in cyclohexane at millisecond time scale. Evolution of Raman bands under dynamic compression reveals crystallization of the sample to cubic (solid-I) phase around 0.8 GPa followed by solid-I (cubic) → solid-III (orthorhombic) transition in the pressure range 1.1–1.7 GPa. On further compression, transition to solid-IV (monoclinic) and solid-V (triclinic) phases are observed in the pressure range 2.7–4.0 GPa and 4.0-5.8 GPa respectively. Our static compression experiments, performed up to 27 GPa, reveal the similar phase transition behavior, contrasting the existing literature. These findings offer new insights into the stability of different high pressure phases of cyclohexane under extreme loading conditions and highlight its potential as a benchmark material for studying phase transition dynamics in molecular systems.

Keywords: Time-resolved Raman Spectroscopy, Phase-transition, Laser-driven shock, Cyclohexane, Energetic materials.

I. Introduction:

The high-pressure behavior of hydrocarbons is pivotal across fields such as condensed matter physics, earth and planetary sciences, and petroleum research [1-5]. Extensive studies have explored the effects of both static [6, 7] and dynamic compression [8-10] on simple unsaturated cyclic hydrocarbons (aromatics) like benzene and hexafluorobenzene. In benzene, dynamic compression lowers the phase transition pressure due to thermal activation at elevated temperatures, while the phase transition pathway remains unchanged [8, 9]. In contrast, hexafluorobenzene exhibits the suppression of an intermediate phase (phase-I) under dynamic compression [10], a phase present in static high pressure conditions [7]. Recently, our group demonstrated that in benzene: hexafluorobenzene co-crystals, high strain rate compression suppresses phase-V and alters phase transition pressures [11]. Despite these advances, the impact of strain rate on phase transitions in saturated cyclic hydrocarbons remains largely uncharted territory.

Cyclohexane (C_6H_{12}), a prototypical saturated cyclic hydrocarbon, is a liquid at room temperature (melting point = 279.6 K). Unlike benzene, which has a delocalized π-electron cloud, cyclohexane contains only σ bonds, making it an intriguing candidate for studying its behavior under both dynamic and static compression. Its inert, non-polar, and transparent nature also makes it a promising hydrostatic medium for diamond anvil cell (DAC) experiments, particularly with reactive materials [12]. Additionally, cyclohexane serves extensively as a solvent, a reaction medium, and as a precursor in nylon synthesis, and its stability makes it a significant component in large biological molecules, such as steroids and carbohydrates [13]. Cyclohexane has also been suggested as a hydrocarbon framework for energetic materials [14], with recent work by Yan et al. demonstrating the potential of cyclohexane-TNT co-crystals as enhanced energetic materials compared to TNT alone [15]. Given its diverse applications, investigating cyclohexane under extreme conditions holds considerable fundamental and applied significance.

Cyclohexane has been extensively studied under hydrostatic compression [1, 12, 16, 17]: Liquid cyclohexane crystallizes in the cubic plastic phase (phase-I) below 0.5 GPa, as indicated by increased Raman peak intensities. At 1.1 GPa, it transitions to an orthorhombic phase (phase-III), marked by the splitting of C-C stretching (ν_{22}), CH_2 twisting (ν_{21}) and CH_2 wagging (ν_{20}) modes with E_g symmetry. Around 2.2 GPa, it transforms into a monoclinic phase (phase-IV), evidenced by further splitting of these modes. Phase-V emerges between 5–5.5 GPa, characterized by distinct changes in C-C stretching (ν_5 & ν_{22}), and CH_2 twisting (ν_{21}) modes, followed by phase-VI between 9.8–12.8 GPa. The molecular unit of cyclohexane persists up to 40 GPa. Upon cooling, it solidifies into a cubic plastic phase (solid-I) around 280 K before transitioning to a monoclinic solid (phase-II) below ~187 K [15]. A few studies have also examined cyclohexane under dynamic compression. Dick et al. [18] were the first to investigate its behavior up to 43 GPa using flyer impact technique, revealing a quadratic relationship between particle and shock velocity. Matsuda et al. [19] conducted *in-situ* time-resolved Raman spectroscopy (TRRS) on laser-shocked cyclohexane up to 1.3 GPa to determine shock velocity. More recently, Yuan et al. [20] used a piezoelectric-actuated diamond anvil cell (d-DAC) with Raman spectroscopy to study cyclohexane under dynamic compression at millisecond time scales, revealing the significant influence of strain rate on phase transitions, which led to the discovery of two novel phases at 2.23 and 3.98 GPa. Given the lower strain rate in d-DAC compression compared to shock-compression techniques (e.g., gas gun, laser-driven shock etc.), further exploration of cyclohexane's phase diagram under shock compression remains compelling.

In recent years, laser-shock compression has emerged as one of the preferred methods of exposing materials to extreme thermodynamic conditions including high-pressure, high-temperature, and extreme strain rates [21-27]. Detecting the changes induced by shock waves requires velocimetric methods (such as photon Doppler velocimetry [28]) for particle velocity measurements as well as *in-situ* time-resolved spectroscopic [29] and diffraction [22] methods that reveal the temporal evolution of a material's vibrational properties and structure.

Our study seeks to address the crucial question: If the phase transition route in cyclohexane can be significantly influenced by compression over the millisecond time scale, what happens to cyclohexane under ultrafast compression? Here, we present *in-situ* nanosecond-TRRS studies of laser-shocked cyclohexane, achieving pressures up to 5.8 GPa, with a focus on identifying shock-induced phase transitions. To substantiate our findings, we also conducted hydrostatic compression experiments and 1-D radiation hydrodynamics simulations.

II. Experimental details:

II a. Dynamic compression experiments:

Dynamic compression experiments were performed at the TRRS facility at the BARC in Mumbai. The facility comprised a 10 J Q-switched Nd:YAG laser with a pulse duration of ~ 8 ns and a wavelength of 1064 nm, a confinement target geometry, and a half-meter Raman spectrometer equipped with an intensified charge-coupled device (ICCD). A second harmonic ‘probe’ beam was derived from a mirror leak of the main beam. It had a pulse width of ~ 6ns and a wavelength of 532 nm. The fundamental beam (or the ‘pump’ beam) was used to generate shock waves in the target material while the probe beam was used to incite Raman scattering in the sample. To capture the temporal changes induced by the propagating shock wave, the delay between the pump and probe beams was adjusted shot-to-shot using a timing-slide. The laser beam had an ~ 80% flat-top spatial profile to ensure that the shock wave was relatively uniform in strength near the center of the target [30].

The target geometry is shown in figure 1. It consisted of a quartz window (diameter = 20 mm, thickness = 2.5 mm) facing the laser, with a 25 µm aluminum foil behind it, secured with UV-cured adhesive. Behind this was a 200 µm thick Teflon spacer, which was filled with the liquid sample under investigation, in this case, cyclohexane. The rear of the target was composed of a second quartz window identical to the front window. In this confined geometry, both the shock pressure and shock lifetime in the cyclohexane were enhanced by factors of ~6 and ~10 respectively [30].

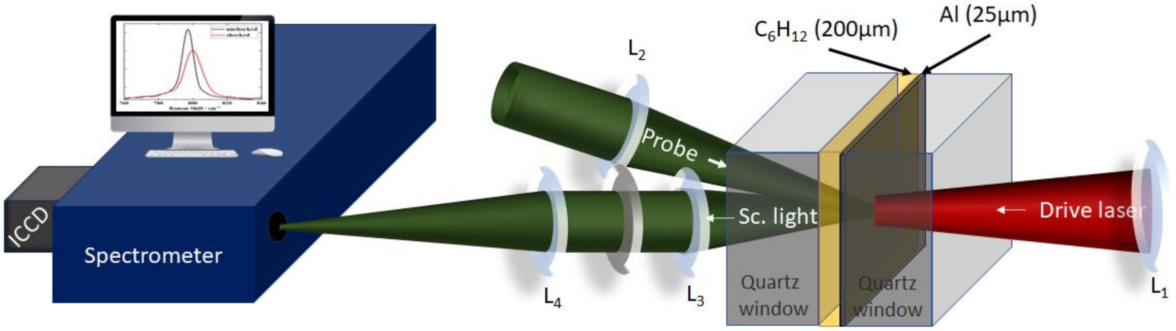

Fig. 1. Schematic of the target geometry used for the experiments. Cyclohexane is a colorless liquid at room temperature and pressure; the yellow color used here is for illustrative purposes only. L_1, L_2, L_3 and L_4 are lenses, F is an edge filter.

The pump beam, focused to a diameter of ~ 1.8 mm at the quartz-aluminum interface, initiates the formation of a backwards-expanding plasma (opposite to the direction of the laser beam) at the interface, resulting in a shock wave being driven into the aluminum in the forward direction. This shockwave then propagated into the cyclohexane sample, compressing it. From the rear side, probe beam was focused to a spot size of ~ 500 µm at the center of the shocked region to incite Raman scattering in the sample.

The scattered light was collected using an f/2 lens and was focused onto the entrance slit of a half-meter Andor SR 500 monochromator using an f/6 lens. The scattered light was detected using an Andor iStar DH340 (2048 × 512 pixels) ICCD with minimum gating time of ~ 1.2 ns. The target assembly was mounted on a computer-controlled X-Y-Z stage enabling exposure of a fresh region of the sample for each new shot. More details about the experimental set-up can be found in our earlier work [30].

II b. Hydrostatic compression experiments:

Hydrostatic compression experiments were performed using a modified Mao-Bell type DAC equipped with a pair of diamonds with culet size ~ 400 µm. The sample chamber was created by drilling a hole of diameter ~100 µm at the centre of an ~ 80 µm thin indented gasket with an initial thickness of ~250 µm. The cyclohexane sample, in its liquid form, was loaded into the sample chamber along with a small ruby speck for pressure calibration. *In-situ* Raman scattering experiments on the hydrostatically compressed cyclohexane were carried out using a triple-stage confocal micro-Raman spectrograph (JobinYvon T64000) in subtractive mode, configured in the single stage setting. The 488 nm wavelength of an Ar ion laser was used as an excitation source for the Raman scattering. A 20× objective lens was used in backscattering geometry to collect the Raman scattered light. Pressure was calibrated using the ruby fluorescence technique [31], as per the following the equation:

$$P(GPa) = 380.8 \left[\left(\frac{\lambda}{\lambda_0}\right)^5 - 1\right] \qquad (1)$$

Where λ is the measured wavelength of the ruby R_1 line and λ_0 = 694.24 nm is the zero-pressure value at 298 K.

III. Simulations:

One-dimensional radiation-hydrodynamics simulations were performed to model the dynamic compression experiments using the HYADES code [32]. HYADES is a Lagrangian radiation-hydrodynamics simulation code, which uses a flux-limited diffusion model of electron transport. A multi-group diffusion approximation was employed to mimic thermal radiation transport within the target, utilizing 40 radiation groups arranged logarithmically from 1 eV to 2 keV. The equations of state (EOS) for quartz and aluminum were taken from the SESAME library [33]. For cyclohexane, due to the unavailability of tabulated high-pressure EOS data and a lack of suitable bulk modulus data for constructing a quotidian EOS, the SESAME EOS for C_XH_{2X} was used as a substitute. This substitution is expected to introduce errors, particularly at lower energies, therefore simulations were only performed for experiments driven by laser energies ≥ 400 mJ. An in-line average-atom LTE model was employed to model ionization in each material region.

IV. Results and analysis:

IV a. <u>Static compression experiments:</u>

Cyclohexane (purity > 99 %) was obtained from Sigma-Aldrich and used as-purchased. Figure 2 and 3 show the evolution of the Raman bands as a function of pressure in the spectral regions 700-1300 cm^{-1} and 2700-3200 cm^{-1} respectively, while figure 4 shows the evolution of the ν_{22} (C-C stretching) mode as a function of pressure in cyclohexane. The Raman mode at ~1444 cm^{-1} at ~0.4 GPa has been omitted from the manuscript due to its weak nature and poor statistical reliability.

The following changes are observed in the Raman spectra of cyclohexane on increasing the pressure: As the pressure is increased to ~0.4 GPa, intensity of Raman bands increases while Full Width at Half Maximum (FWHM) decreases (see figures 2a, 3a and 4a), indicating crystallization of the sample. This crystalline phase is classified as a cubic plastic phase (solid phase I; s. g. Fm3m), characterized by dynamic molecular disorder, where the molecules undergo rapid reorientations at their lattice sites [1, 34].

At 1.3 GPa, the ν_{23} mode (CH_2 rocking mode, observed at ~800 cm^{-1} at ~0.1 GPa) develops a pre-shoulder peak. With compression, the ν_{22} mode (C-C stretching mode, observed at ~1027 cm^{-1} at 0.1 GPa) stiffens to ~1035 cm^{-1} and shows considerable broadening at 0.9 GPa as seen in figure 4a. On further compression to ~1.3 GPa, this mode develops a post shoulder peak along with the emergence of a new Raman peak at ~1286 cm^{-1} (near ν_{21} Raman mode). In the C-H spectral region (2700- 3300 cm^{-1}), primarily four Raman modes ν_1, ν_{17} (CH_2 anti symmetric (as)), ν_2, ν_{18} (CH_2 Symmetric stretching (ss)) are observed at ~2941, ~2926, ~2855 and ~2893 cm^{-1} respectively, at ~0.1 GPa (figure 3). At 0.9 GPa, a weak Raman peak emerges at ~2925 cm^{-1}. With further compression to 1.3 GPa, the symmetric and antisymmetric stretching modes stiffen and the new Raman mode gains intensity at the expense of the other modes. These spectral changes collectively indicate transition from high symmetry cubic phase (solid phase I) to a lower symmetry orthorhombic (solid phase III; s. g. Pmnn) phase [1]. This high-pressure phase (solid phase III) shares structural similarities with metastable monoclinic phase (solid phase II), observed at low temperatures (below T =186.1 K [35]). The transition involves an order-disorder mechanism in which molecules adopt an orientationally ordered 'chair-like' conformation. Notably, the molecular packing in this phase is more complex, requiring greater cooperative behavior among neighboring molecules.

As pressure increases, significant spectral changes are observed in various Raman modes. Upon compression to 1.8 GPa, the ν_{23} mode splits into two Raman modes at ~811 cm^{-1} and ~814 cm^{-1}. Simultaneously, the ν_{22} mode splits into two peaks (at ~1039 cm^{-1} and ~1045 cm^{-1}) (figure 4a). Concomitantly, two weak Raman modes emerge at ~1031 cm^{-1} and at ~1070 cm^{-1} around the ν_{22} mode. At the same pressure, the three Raman peaks near the ν_{21} mode (1265 cm^{-1} at 0.1 GPa) further split into four peaks. In the C-H region, the new Raman peak at ~2925 cm^{-1} splits into two peaks at ~2935cm^{-1} and ~2942 cm^{-1}, as seen in the figures 3 and 5b. These spectral changes corroborate with previously published results [1] and indicate the transition from solid phase III (orthorhombic) to a lower symmetry solid phase IV (monoclinic) at 1.8 GPa. Structurally, the phase IV closely resembles the phase III, with nearly identical lattice parameters and atomic coordinates, except for the monoclinic distortion of the β-angle from 90° to 97.108° [36]. The relationship between phase III (s. g. Pmnn) and phase IV (s. g. $P12_1/n1$) is defined by a group-subgroup transformation with the molecular orientations in both phase being closely related. The transition from phase III to phase IV can therefore be attributed to molecular rotation in alignment with the monoclinic distortion of ~7°.

Upon further compression to 3.0 GPa, the relative intensity of the pre-shoulder peak at ~816 cm^{-1} increases compared to the CH_2 bending mode at ~819 cm^{-1}. The primary ν_{22} C-C stretching mode at ~1039 cm^{-1} (at 1.8 GPa) begins to split into two Raman peaks at ~1043 cm^{-1} and ~1046 cm^{-1} at 3.0 GPa. This suggests a reduction in site symmetry, resulting in generation of nonequivalent Wyckoff sites in the high-pressure phase. A new Raman peak also appears at ~1124 cm^{-1}. Additionally, intensity redistribution occurs among the C-H symmetric and asymmetric stretching modes, accompanied by the emergence of a weak Raman peak at ~3082 cm^{-1}. The relative intensity of the 2967 cm^{-1} peak increases with respect to the 2977 cm^{-1} peak.

As the pressure is further increased, gradual changes are observed up to 5.0 GPa. At 7.8 GPa, the ν_{23} Raman mode (CH_2 bend) stiffens along with its pre-shoulder peak, and its intensity reduces substantially. In the C-C stretching region, intensity redistribution occurs between the ν_{22} mode (C-C stretch) and the new Raman mode at ~1060 cm^{-1}, with both reaching equal intensity at 7.8 GPa. In the C-H stretching region, the intensity redistribution happens between the C-H asymmetric modes. At this pressure, the intensity of the Raman mode at ~2945 cm^{-1} increases drastically. These spectral changes indicate another structural phase transition from the solid phase IV to a phase of even lower symmetry, the solid phase V (triclinic; s. g. P1) [1, 12, 37].

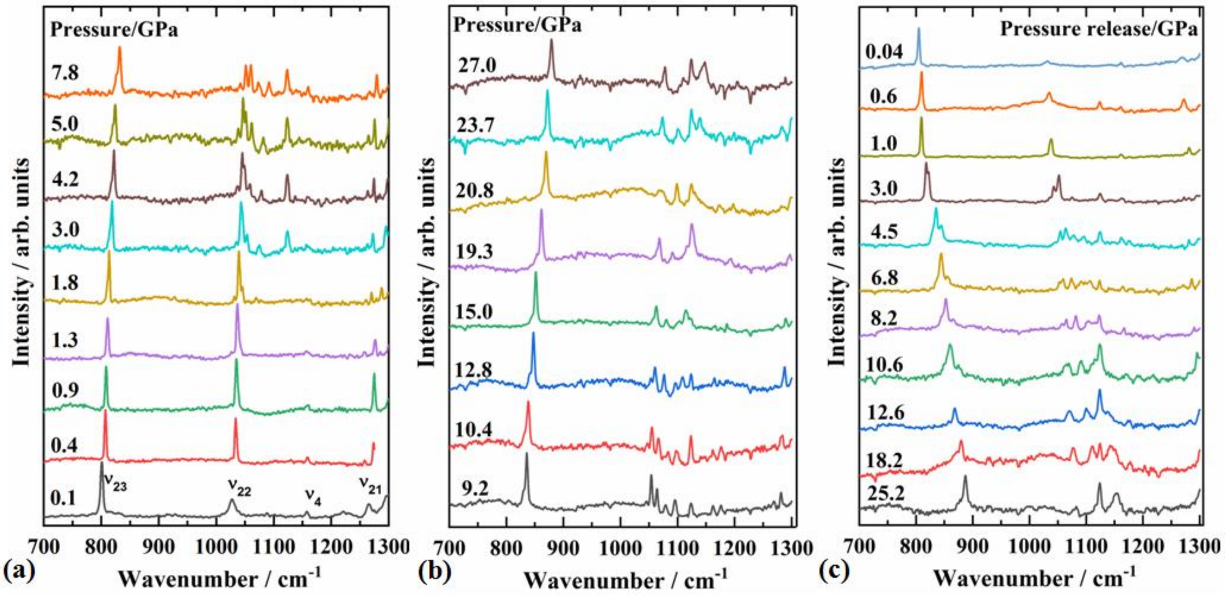

Fig. 2. Raman spectra of cyclohexane stacked at a few representative pressures in the spectral region 700-1300 cm^{-1} (static compression).

With further compression, several new modes emerge in the C-C stretching region (1000 - 1350 cm^{-1}), as shown in figure 4b. In the C-H stretching region, at 9.2 GPa, the weaker Raman mode at ~2963 cm^{-1}, adjacent to the stronger Raman mode at ~2950 cm^{-1}, gains intensity with compression, and these two Raman modes become comparable in intensity by 12.8 GPa. The C-H asymmetric stretching modes show pronounced stiffening with pressure, indicating a significant change in the electronic density distribution within the cyclohexane molecule. These spectral changes indicate another structural transition from the solid phase V to solid phase VI [1, 12]. Both these phases are iso-symmetric in nature (triclinic; s. g. P1) [37].

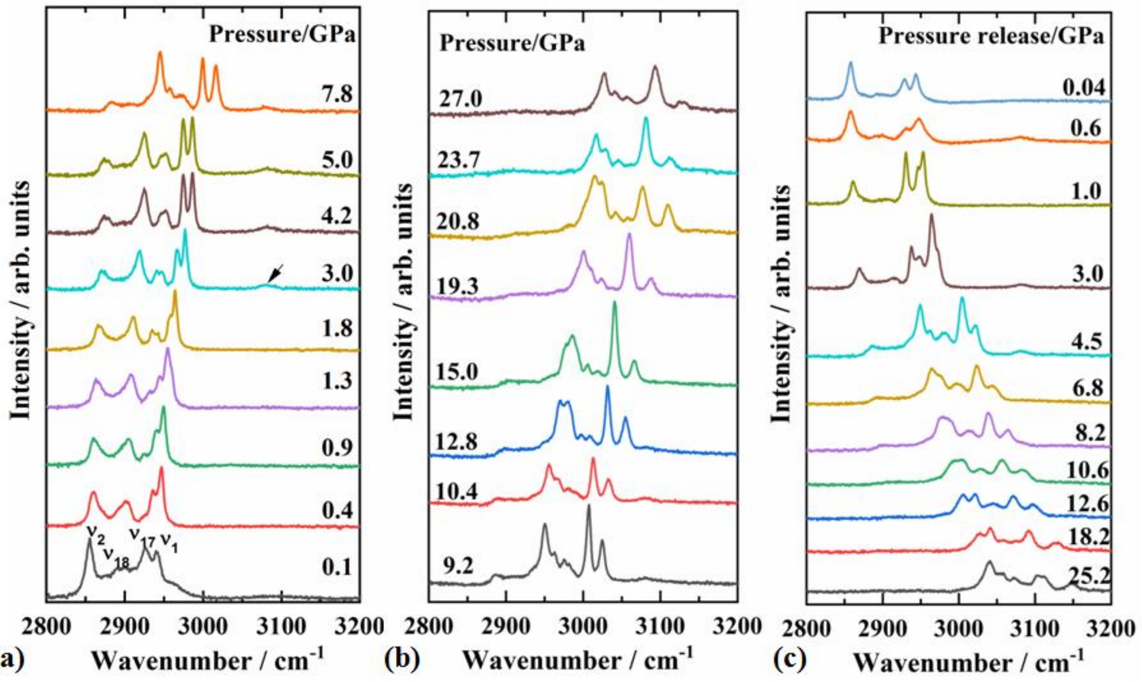

Fig. 3. Raman spectra of Cyclohexane stacked at a few representative pressures in the spectral region 2700-3200 cm^{-1} (static compression).

Upon further compression to 19.3 GPa, in addition to the expected modes stiffening, the Raman mode at ~1125 cm^{-1} (C-C stretching region) and Raman modes at ~3000 cm^{-1} and ~3059 cm^{-1} (C-H stretching region) become quite intense. The discontinuity observed in the frequency vs. pressure plot (figure 5) around this pressure suggests the possibility of another structural variation at ~19.3 GPa.

At 20.8 GPa, the Raman mode at ~1072 cm^{-1} broadens significantly but narrows again with increasing pressure, showing a ~6 cm^{-1} stiffening at ~27 GPa. At this highest pressure, the symmetric stretching mode at 3028 cm^{-1} appears as a sharp peak, while the asymmetric stretching mode at 3094 cm^{-1} exhibits considerable broadening. Additionally, the other asymmetric stretching mode shows splitting into two distinct Raman modes at ~3125 cm^{-1} and ~3131 cm^{-1}. Upon releasing the pressure from 27 GPa, characteristic spectral signatures of various high pressure phases reappear within their respective pressure ranges (figures 2c, 3c and 4c). Upon complete decompression, all Raman bands revert to their original positions (topmost pattern in figures 2c, 3c and 4c), confirming the fully reversible nature of the phase transitions.

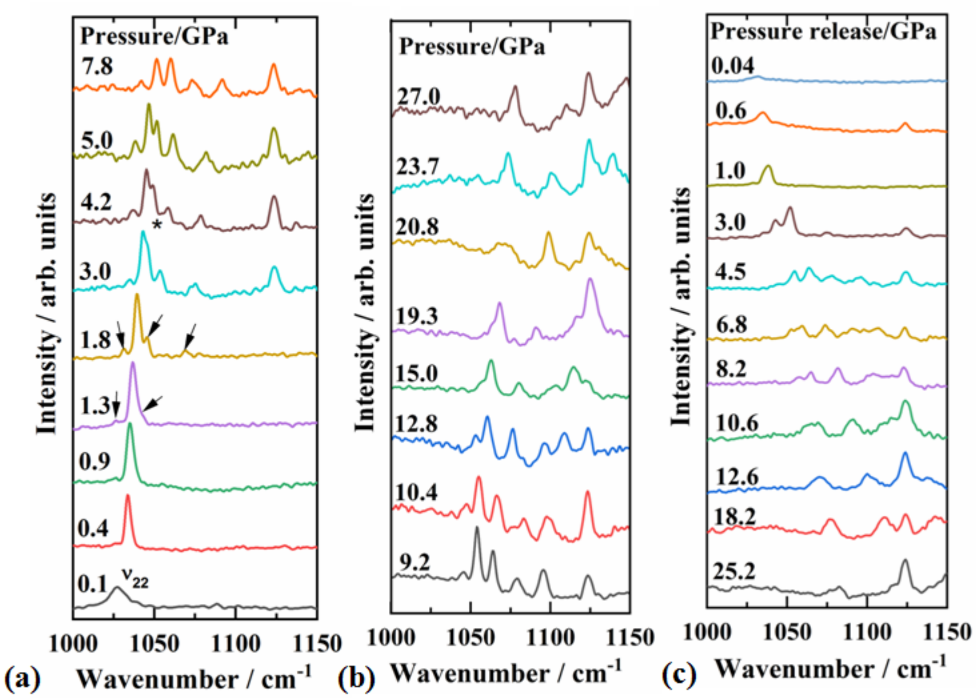

Fig. 4. Enlarged view of Raman spectra in the spectral region 1000-1150 cm^{-1} (Static compression).

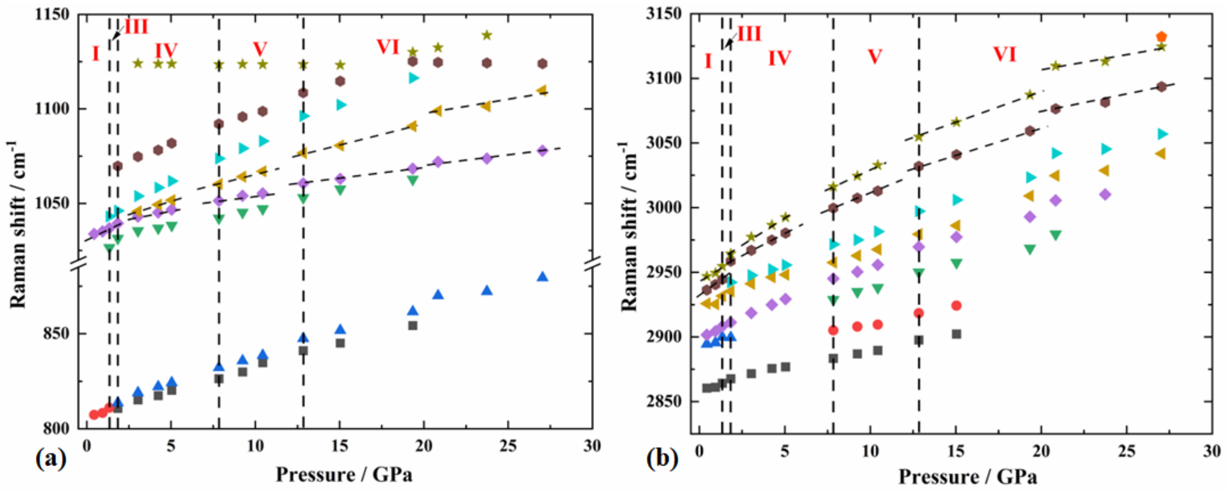

Fig. 5. Variation of Raman mode frequencies with pressure (Static compression).

In the following sections, we discuss the evolution of Raman bands of cyclohexane as a function of delay and shock pressure, as obtained using laser-driven shock and *in-situ* time resolved Raman spectroscopy. These results are, then, compared with findings from the quasi-hydrostatic experiments discussed earlier.

IV b. <u>Shock compression experiments</u>:

Shock compression experiments were conducted in two phases. In the first phase, the pump (400 mJ) and probe energies (5 mJ) were fixed while the delay between the two was varied from 10 ns to 94 ns in steps of 7 ns and 14 ns. Here, t = 0 ns corresponds to the moment when pump and probe beams simultaneously reach the aluminum – quartz interface. This approach allowed us to track the propagation of the shock wave within the sample and determine its velocity and consequently, the shock pressure. Due to the relatively weak Raman signal from the sample at ns timescale, each measurement required accumulating 75 shots per delay, with a gating time of 3 ns per shot, yielding a total collection time of 225 ns. The acquired Raman spectrum has contributions from both the shocked and unshocked regions of the sample. To discern the respective influences of these regions, a multi-Lorentzian peak-fitting technique was employed. In this approach, the FWHM and position of the first peak were constrained to match those of the unshocked Raman peak, while the parameters of the remaining peaks were allowed to vary for optimal fitting. The results were then analyzed to determine the fractional distance traveled by the shock wave as a function of time delay, providing an estimate of the shock velocity in the sample.

In the second phase of the experiment, the delay between the pump and the probe beams was fixed, while the pump energy was systematically varied from 40 mJ (0.20 GW/cm^2) to 1600 mJ (7.90 GW/cm^2), enabling control over the shock pressure in the sample from 0.5 GPa to 5.8 GPa. The energy of the probe beam was kept at 5 mJ throughout the experiment. To enhance the signal-to-noise ratio in this phase, 120 shots were taken at each shock pressure, with a gating time of 5 ns, resulting in total accumulation time of 600 ns. The same peak-fitting procedure was employed as in the first phase.

IV b (i). <u>Time delay analysis & calculation of shock wave velocity</u>:

To gain a better understanding of the shock wave hydrodynamics in the sample and to validate the simulations, a series of time-delay measurements were conducted at a pump energy of 400 mJ (I ~ 2.0 GW/cm^2). The delay between the pump and probe beams was varied in increments of 7 ns or 14 ns. Three prominent Raman modes— ν_{23} (CH_2 rocking mode), ν_{22} (C-C stretching mode), and ν_{21} (CH_2 twisting mode) — were monitored to determine the shock velocity at 400 mJ. Figures 6a and 6b present the analysis of the ν_{23} and ν_{22} modes, respectively, while figure 6c shows the simulated shock wave profiles at various delays. The experimental peaks have been color-matched with the unshocked and shocked regions in the simulation results to facilitate more straightforward interpretation.

At a 10 ns delay, the experimental Raman spectra (figure 6a and 6b) show no observable change, consistent with the simulation results at 12 ns (figure 6c), which indicate that the shock wave has just entered the sample. This suggests that at 10 ns, the shock wave remains confined within the aluminum. On increasing the delay to 24 ns, a new peak (green in figures 6a and 6b) appears at a higher wavenumber, indicating that the shock wave has entered the sample and travelled some distance into it (green region in figure 6c). The emergence of this higher-wavenumber peak signifies the stiffening of the Raman modes under shock compression. The relatively low intensity of the green peak suggests that the shock wave has travelled a very small distance in the sample and majority of the sample remains unshocked. As the delay is further increased, the shock wave penetrates deeper into the sample, causing the intensity of the shocked peak to grow. However, as the shock wave propagates further, its strength gradually diminishes since it is no longer being reinforced after the end of the pump pulse. Consequently, the shocked peaks at longer delays exhibit redshift. At a delay of 66 ns, the original unshocked Raman peak disappears for both ν_{23} and ν_{22} modes and a new, smaller peak (burgundy color) appears at an even higher wavenumber. This suggests that the shock wave has likely traversed the entire sample thickness within ~ 62-64 ns. Additionally, due to impedance mismatch (as the shock impedance of quartz is higher than that of cyclohexane), a reflected shock wave with a higher amplitude propagates back into the sample (represented by the burgundy region in figure 6c). This leads to the formation of a new peak at an even higher frequency. The simulation results in figure 6c confirm that the shock wave reaches the sample boundary at ~ 62 ns. The region affected by the reflected shock wave (burgundy region in figure 6c) experiences double compression, resulting in overall higher pressure, which manifests as the new Raman peak at a higher wavenumber. As the delay is further increased to 80 ns and 94 ns, both the green- and burgundy-colored peaks undergo redshift due to the rapid decay of the reflected shock wave as it propagates through the rarefaction wave generated by the forward-moving shock wave. By 94 ns, figures 6a and 6b show that the green peak has nearly shifted back to the position of the initial unshocked signal. This suggests that the singly shocked region (green) is overtaken by the rarefaction wave, effectively restoring the sample to a near-unshocked state, as evidenced by the shock pressure in cyclohexane at 94 ns (green region in figure 6c). These observations highlight the reversible nature of the changes induced by the shock wave in cyclohexane.

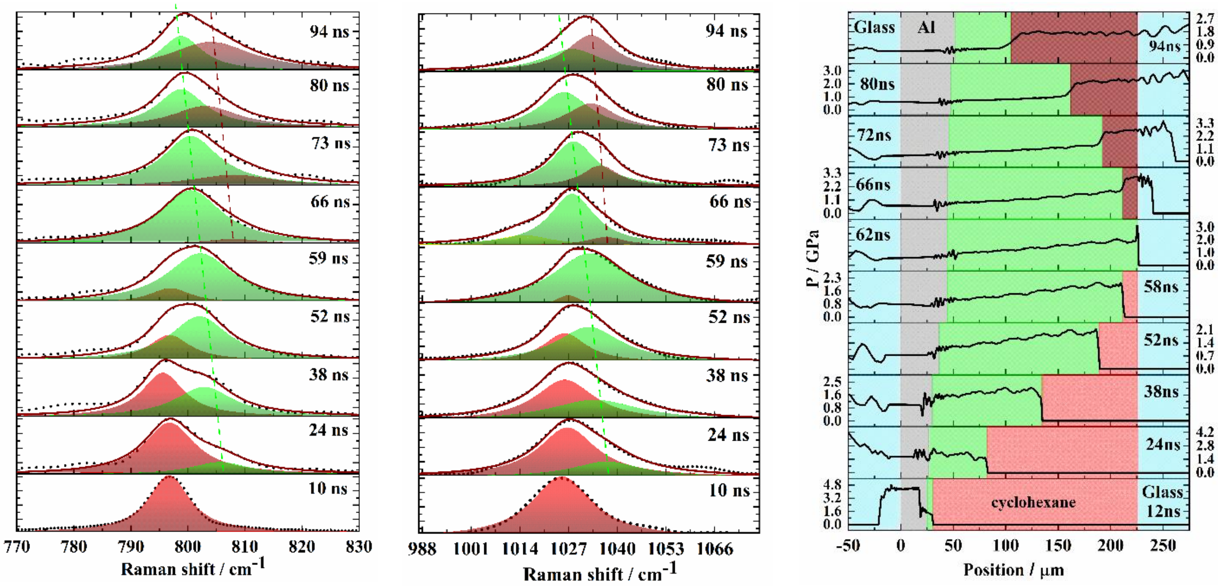

Fig. 6. Lorentzian fit of the shocked **(a)** ν_{23} (CH_2 rocking mode) mode and **(b)** ν_{22} (C-C stretching mode) mode for different delay times at 400 mJ. **(c)** The spatial profile of shock waves at different delay times for a laser energy of 400 mJ (obtained from 1D radiation-hydrodynamics simulations). The red, green,

and burgundy colors correspond to unshocked, shocked, and doubly/re-shocked regions, respectively (both in peak fitting and in simulation results).

In addition, we determined the shock wave velocity (U_s) by analyzing both experimental and simulation results. Experimentally, U_s was calculated using the equation $U_s = r.d$ [38] where 'd' is the sample thickness (200 μm) and 'r' is the slope of the intensity ratio $I_{shocked}/(I_{shocked} + I_{unshocked})$ *vs.* the time delay curve (figure 7a). The intensities $I_{unshocked}$ and $I_{shocked}$ were obtained through Lorentzian curve fitting of the experimental data, as detailed in figures 6a and 6b. In simulations, U_s was determined from the slope of the shock wave's fractional volume coverage ($V_{covered} / V_{total}$) plotted against time delay (figure 7a). This analysis leverages the direct relationship between Raman mode intensity and sample volume, incorporating the sample thickness as a multiplier.

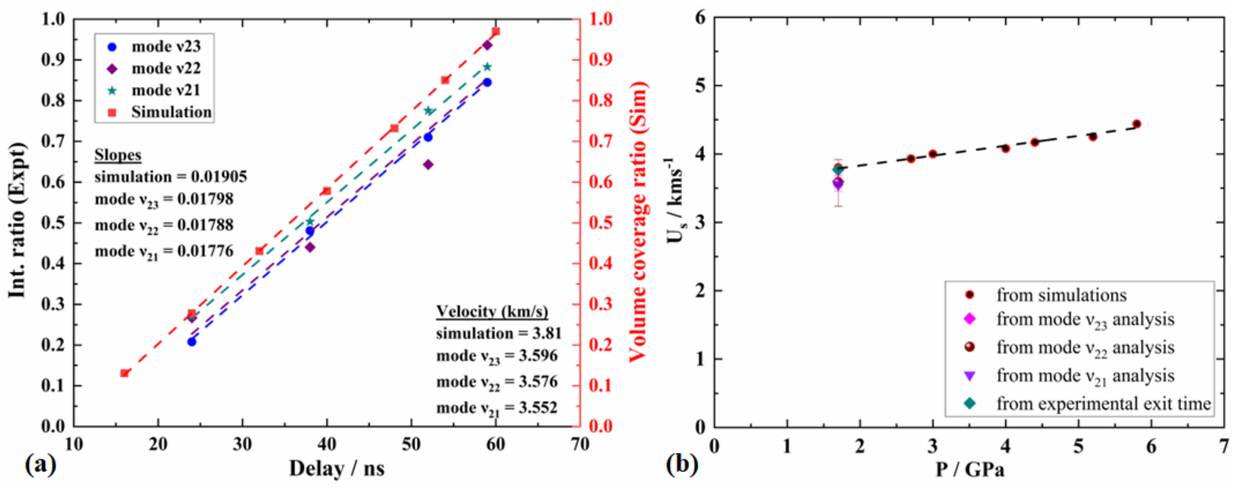

Fig. 7. (a) The slope of the graph from the experimental (ν_{23}, ν_{22}, and ν_{21} modes) and simulation results is a direct measure of U_s, here shown at laser energy of 400 mJ. **(b)** The variation in U_s with pressure (the straight dotted line is a linear fit to the simulation results as a guide to eyes).

At 400 mJ, the experimentally obtained U_s are 3.596 ± 0.095 km/s (ν_{23} mode), 3.576 ± 0.341 km/s (ν_{22} mode) and 3.552 ± 0.096 km/s (ν_{21} mode) which closely match the U_s obtained from the simulation i.e. 3.810 ± 0.022 km/s. The slightly higher simulated velocity is expected due to the absence of two-dimensional edge-loss effects in the 1D simulations. Figure 7b illustrates the relationship between U_s and shock pressure. Given the high cost of time-resolved measurements for each data point, the shock velocities (and hence the shock pressure) in the sample at other laser energies were obtained from the simulation results.

IV b (ii). Evolution of Raman spectra under varying shock pressure:

In the second phase of our experiments, we conducted dynamic compression studies by applying incremental shock pressures ranging from 0.5 GPa to 5.8 GPa, achieved by adjusting the laser energy between 40 mJ and 1.6 J. The objective was to investigate the effects of ultrafast dynamic compression on the phase diagram of cyclohexane.

At shock pressure of 0.5 GPa, we observe subtle broadening of the Raman modes towards higher frequencies, indicating a blue shift with increasing pressure. Additionally, the intensity of these modes in the shocked state is comparatively lower than that of the unshocked signal. As the pressure is increased to 0.8 GPa, a significant increase in signal intensity is observed relative to the unshocked signal (figure 8a), signaling the transition from the liquid to solid phase I (cubic plastic phase). Under static compression, this phase transition occurs below 0.4 GPa, followed by a transition to solid phase III around 1.3 GPa.

At a shock pressure of 0.8 GPa, we observe a new peak at 1437 cm^{-1} which becomes more prominent at ~1.1 GPa. However, no additional spectral changes indicative of the solid phase III are discernible at this pressure. When the shock pressure is increased to 1.7 GPa, the ν_4 mode (CH_2 rocking mode at 1157 cm^{-1}) exhibits splitting, forming a small shoulder peak at 1149 cm^{-1}. Additionally, the ν_{22} (C-C stretching) mode splits into two, and a new Raman peak appears at 1068 cm^{-1}. These spectral changes are consistent with the solid I to solid III phase transition observed in static compression experiments. Based on our findings, within our experimental framework, the transition from the solid phase I to the solid phase III commences at 0.8 GPa and completes at 1.7 GPa. Thus far, our dynamic compression results align with both our static compression data and previously reported static compression studies, albeit at higher pressure [1, 12].

Upon further increasing the shock pressure to 2.7 GPa, new Raman modes appear at ~1020 cm^{-1}, 1281cm^{-1}, and 1432 cm^{-1}. Under static compression, the solid III to solid IV phase transition occurs around 1.8 GPa and is associated with the emergence of several new Raman modes at 788 cm^{-1}, 1043 cm^{-1}, 1067 cm^{-1}, 1268 cm^{-1}, 1285 cm^{-1}, and 1449 cm^{-1} [1, 12]. In our shock compression experiments, we did not detect a Raman peak at 788 cm^{-1}, likely due to its inherently low intensity.

However, we did observe peaks at 1043 cm^{-1} and 1067 cm^{-1} at a shock pressure of 1.7 GPa, and peaks at 1268 cm^{-1} and 1285 cm^{-1} at a shock pressure of 2.7 GPa. The Raman peak at 1449 cm^{-1} appears to have merged with the unshocked Raman peak. These findings collectively indicate a transition from solid phase III to solid phase IV. Interestingly, this contrasts with the ms-scale dynamic compression results reported by Yuan et al. [20], where the authors claim to have identified a novel phase, designated as solid IV', instead of the conventional solid phase IV, at a similar pressure. Notably, the dynamic compression Raman spectra reported by Yuan et al. [20] closely resemble the spectra obtained in both our dynamic and static compression experiments, as well as previously published static compression results [12, 16, 17]. However, their static compression Raman spectra show significant discrepancies compared to our results and prior static compression studies [12, 16], leading them to assert that their dynamic compression results diverge from the static compression data. Consequently, they proposed a novel phase labeled as IV', different from the previously established phase IV.

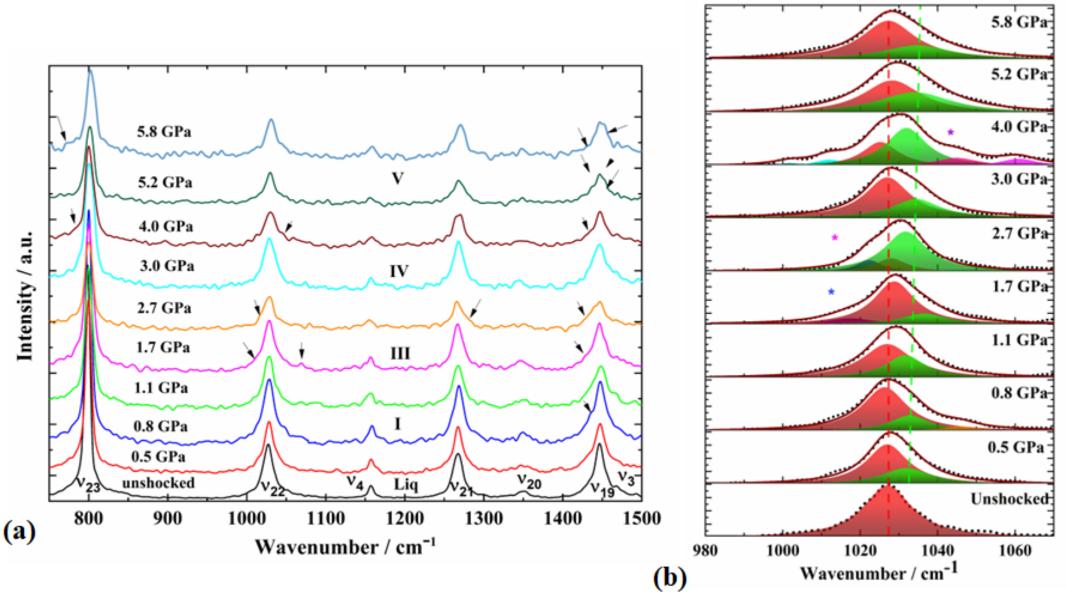

Fig. 8. (a) Evolution of Raman spectra of cyclohexane in the region 700 – 1500 cm^{-1} as a function of shock pressure. Indicators mark the positions of changes in the Raman peaks. **(b)** Lorentzian peak fitting of ν_{22} (C-C stretching) Raman mode. Red peaks correspond to the unshocked region and other colors correspond to different shocked peaks (dynamic compression).

As the shock pressure increases to 4.0 GPa, three new Raman modes emerge at 1044 cm^{-1}, 1435 cm^{-1}, and 1455 cm^{-1}, becoming distinctly discernible at 5.2 GPa and 5.8 GPa. This marks the onset of the transition from the solid phase IV to the solid phase V phase between 4.0 GPa to 5.8 GPa. Pravica et al. [12] observed only the splitting of the ν_{22} peak near 1035 cm^{-1} between 2.76 GPa and 3.5 GPa, attributing it to Fermi resonance of an infrared mode overtone rather than a phase transition. In contrast, Crains et al., [16] reported the splitting of the ν_5 mode, with a shoulder peak on the higher frequency side, alongside the splitting of ν_{22} mode, which they unequivocally identified as solid phase V. Yang et al. [1], confirmed the phase transition from solid phase IV to solid phase V by detecting new Raman peaks at 787 cm^{-1}, 1155 cm^{-1}, and 1437 cm^{-1} at 4.6 GPa. Upon further compression, they observed additional peaks at 1376 cm^{-1}, 1438 cm^{-1}, 1453 cm^{-1}, and 2969 cm^{-1}. Baonza et al. [17] also reported a phase transition at 3.2 GPa, indicated by the splitting of the ν_5 and ν_{21} modes. Based on our findings and corroborating evidence, we concur that the Fermi resonance observed between 2.7 and 5.2 GPa by Pravica et al. [12] indeed signifies a genuine phase transition from solid phase IV to solid phase V. In their ms-timescale dynamic compression study, Yuan et al. [20] reported a potential transition to a new phase V' (distinct from solid phase V), at 3.98 GPa, characterized by the splitting of the ν_{19} (1444 cm^{-1}) and ν_{22} (1037 cm^{-1}) peaks and the emergence of new peaks at 1435 cm^{-1} and 1047 cm^{-1}. However, our results, consistent with static compression results, indicate the presence of phase V rather than phase V' during ns-timescale dynamic compression.

In summary, our dynamic compression results closely align with both our static compression findings and previous static compression studies [1, 12, 16, 17], with minor variations in phase transition pressures. This discrepancy may be attributed to the elevated temperatures associated with laser-shock experiments. Furthermore, upon closer examination, the new phases reported by Yuan et al. [20] under dynamic compression closely resemble those observed in our study and previous static compression studies [1, 12, 16, 17]. Based on these observations, we conclude that strain rate does not influence the phase transition pathway of cyclohexane.

Additionally, Raman spectra of the shock-recovered sample confirmed the reversibility of phase transitions. However, in-situ time-resolved Raman spectroscopy during unloading was not feasible due to experimental constraints, including the high cost associated with the destructive nature of the experiments, rear window damage preventing Raman signal acquisition, and probe beam pointing instability at longer delays (necessary for complete shock release) leading to misalignment between the pump and probe beams. Given the valuable insights decompression kinetics and phase hysteresis can provide, future studies exploring cyclohexane during shock unloading would be highly valuable.

V. Conclusion:

We conducted in-situ TRRS on laser-shocked cyclohexane to determine its shock velocity. The shock velocity derived from TRRS is in congruence with predictions from our 1D radiation hydrodynamics simulations. Additionally, we performed both static and dynamic compression experiments to investigate the high pressure phases of cyclohexane. Our dynamic compression experiments reveal a sequence of phase transitions: liquid → solid I → solid III → solid IV → solid V phase transitions at 0.8 GPa, 1.1-1.7 GPa, 2.7-4.0 GPa, 4.0-5.8 GPa respectively. A similar phase transition sequence was obtained in our static compression experiments, contrasting the existing literature. However, the transition pressures in dynamic compression experiments are higher than those in static experiments, likely due to the elevated temperatures associated with laser-driven shock compression. Overall, our findings confirm that the phase transition pathway in cyclohexane remains uninfluenced by strain rate.

Acknowledgements:

The authors are grateful to Shri D. S. Munda for his support during the experiments. The authors are also grateful to Dr. S. M. Yusuf, Director, Physics Group, BARC Mumbai for his encouragement during this work.

Data availability statement:

The data that support the findings of this study are available within the article.

References

1. X. Yang, Y. Li, Y. Wang, H. Zhang, K. Li, and H. Mao, "Chemical transformations of n-hexane and cyclohexane under the upper mantle conditions", *Geoscience Frontiers* **12**, 1010 (2021). DOI: https://doi.org/10.1016/j.gsf.2020.06.006
2. M. C. Akin, and R. Chau, "Observation on shock induced chemistry of cyclohexane", *J. Chem. Phys.* **139**, 024502 (2013). DOI: https://doi.org/10.1063/1.4812374
3. A. Y. Kolesnikov, J. M. Saul, and V. G. Kutcherov, "Chemistry of hydrocarbons under extreme thermobaric conditions", *Chemistry Select* **2**, 1336 (2017). DOI: https://doi.org/10.1002/slct.201601123
4. R. Hou, and D. Pan, "Raman spectra of hydrocarbons under extreme conditions of pressure and temperature: a first-principles study" *J. Phys. D: Appl. Phys.* **55**, 044003 (2022). DOI: 10.1088/1361-6463/ac2d65
5. B. A. Al-Mur, A. Pugazhendi, and M. T. Jamal, "Application of integrated extremophilic (halo-alkalo-thermophilic) bacterial consortium in the degradation of petroleum hydrocarbons and treatment of petroleum refinery wastewater under extreme condition", *Journal of Hazardous materials* **413**, 125351 (2021). DOI: https://doi.org/10.1016/j.jhazmat.2021.125351
6. L. Ciabini, F. A. Gorelli, M. Santoro, R. Bini, V. Schettino, and M. Mezouar, "High-pressure and high-temperature equation of state and phase diagram of solid benzene", *Physical Review B* **72**, 094108 (2005). DOI: https://doi.org/10.1103/PhysRevB.72.094108
7. M. Pravica, D. Sneed, Y. Wang, Q. Smith, and M. White, "Hexafluorobenzene under Extreme Conditions" *J. Phys. Chem. B* **120**, 2854 (2016). DOI: http://dx.doi.org/10.1021/acs.jpcb.6b00497
8. U. Rao, S. Chaurasia, A. K. Mishra, and J. Pasley, "Phase transitions in benzene under dynamic and static compression" *J. Raman Spec.* **52(3)**, 770 (2021). DOI: https://doi.org/10.1002/jrs.6047
9. C. Yuan, J. Wang, Q. Yang, S. Feng, X. Zhu, K. Yang, and L. Su, "Phase transition behavior of benzene under dynamic compression: A stable precocious phase" *J. Mol. Liq.* **411**, 125706 (2024). DOI: https://doi.org/10.1016/j.molliq.2024.125706
10. A. Mohan, S. Chaurasia, U. Rao, and J. Pasley, "Time-resolved Raman spectroscopy of hexafluorobenzene (C_6F_6) under laser-driven shock compression" *J. Quant. Spec. Rad. Trans.* **263**, 107547 (2021). DOI: https://doi.org/10.1016/j.jqsrt.2021.107547
11. A. Mohan, S. Chaurasia, and J. Pasley, "Crystallization and phase transitions of C6H6:C6F6 complex under extreme conditions using laser-driven shock" *J. Appl. Phys.* **131**, 115903 (2022). DOI: https://doi.org/10.1063/5.0084920
12. M. G. Pravica, Y. Shen, and M. F. Nicol, "High pressure Raman spectroscopic study of structural polymorphism in cyclohexane", *Appl. Phys. Lett.* **84**, 5452 (2004). DOI: http://dx.doi.org/10.1063/1.1767960
13. Wade, L.G., Jr. Organic Chemistry, 5th ed.; Prentice Hall: New York, 2003.

14. J. Zhou, J. Zhang, B. Wang, L. Qiu, R. Xu, and A. B. Sheremetev, “Recent synthetic efforts towards high energy density materials: How to design high-performance energetic structures?”, *FirePhysChem* **2**, 83 (2022). DOI: https://doi.org/10.1016/j.fpc.2021.09.005
15. Y. Li, and D. Hong, “Two energetic cocrystals of TNT/cyclohexane and picric acid/triethylamine”, *Acta Cryst.* **A74**, A142 (2018). DOI: http://dx.doi.org/10.1107/S0108767318098574
16. J. Crain, W. C. K. Poon, A. C. Smith, and P. D. Hatton, “High-Pressure Raman spectroscopic study of cyclohexane C_6H_{12} and C_6D_{12}” *J. Phys. Chem.* **96**, 8168 (1992). DOI: https://doi.org/10.1021/j100199a064
17. V. G. Baonza, “Phase transitions in cyclohexane up to 10 GPa”, *Chem. Phys. Lett.* **398**, 175 (2004). DOI: https://doi.org/10.1016/j.cplett.2004.09.049
18. R. D. Dick, “Shock compression data for liquids. I. Six hydrocarbon compounds”, *J. Chem. Phys.* **71**, 3203 (1979). DOI: https://doi.org/10.1063/1.438767
19. A. Matsuda, K. G. Nakamura, and K. Kondo, “Time-resolved Raman spectroscopy of benzene and cyclohexane under laser-driven shock compression”, *Phys. Rev. B* **65**, 174116 (2002). DOI: http://dx.doi.org/10.1103/PhysRevB.65.174116
20. C. Yuan, J. Wang, X. Zhang, Y. Xu, S. Feng, and H. Li, “Influence of dynamic compression on the phase transition of cyclohexane”, *J. Mol. Liq.* **363**, 119836 (2022). DOI: https://doi.org/10.1016/j.molliq.2022.119836
21. M. H. Key, “Physics at very high pressures with laser-driven shock waves”, Nature. **283**, 715 (1980). DOI: 0028-0836/80/08715-01$01.00
22. S. Pandolfi, S. B. Brown, P. G. Stubley, A. Higginbotham, C. A. Bolme, H. J. Lee, B. Nagler, E. Galtier, R. L. Sandberg, W. Yang, W. L. Mao, J. S. Wark, and A. E. Gleason, “Atomistic deformation mechanism of silicon under laser-driven shock compression”, *Nat. Comm.* **13**, 5535 (2022). DOI: https://doi.org/10.1038/s41467-022-33220-0
23. R. G. Kraus, R. J. Hemley, S. J. Ali, J. L. Belof, L. X. Benedict, J. Bernier, D. Braun, R. E. Cohen, G. W. Collins, F. Coppari, M. P. Desjarlais, D. Fratanduono, S. Hamel, A. Krygier, A. Lazicki, J. Mcnaney, M. Millot, P. C. Myint, M. G. Newman, J. R. Rygg, D. M. Sterbentz, S. T. Stewart, L. Stixrude, D. C. Swift, C. Wehrenberg, and J. H. Eggert, “Measuring the melting curve of iron at super-Earth core conditions”, *Science.* **375**, 202 (2022). DOI: https://doi.org/10.1126/science.abm1472
24. S. Chaurasia, U. Rao, and A. Mohan, “Para-xylene under extreme conditions: A Raman spectroscopic study”, *J. Raman Spec.* **52(6)**, 1212 (2021). DOI: https://doi.org/10.1002/jrs.6095
25. Z. He, M. Rodel et al., “Diamond formation kinetics in shock-compressed C─H─O samples recorded by small-angle x-ray scattering and x-ray diffraction”, *Sci. Adv.* **8**, eabo0617 (2022). DOI: https://doi.org/10.1126/sciadv.abo0617
26. S. Chaurasia, U. Rao, A. Mohan, and J. Pasley, “Measurement of shock velocity and temperature in laser-shocked carbon disulphide using time-resolved Raman spectroscopy” *J. Quant. Spec. Rad. Trans.* **277**, 108000 (2022). DOI: https://doi.org/10.1016/j.jqsrt.2021.108000

27. T. S. Duffy, and R. F. Smith, "Ultra-High Pressure Dynamic Compression of Geological Materials", *Front. Earth Sci.* **7(23)**, 1 (2019). DOI: https://doi.org/10.3389/feart.2019.00023
28. S. Chaurasia, A. Mohan, A. K. Poswal, and J. Pasley, "High-speed photon Doppler velocimetry for laser-driven flyer acceleration studies" *Pramana – J. Phys.* **96**, 103 (2022). DOI: https://doi.org/10.1007/s12043-022-02340-z
29. S. Chaurasia, A. Mohan, A. K. Mishra, C. D. Sijoy, and V. Mishra, "In situ time-resolved Raman spectroscopy of nitromethane under static and dynamic compression" *J. Appl. Phys.* **134**, 085901 (2023). DOI: https://doi.org/10.1063/5.0155484
30. S. Chaurasia, V. Rastogi, U. Rao, C. D. Sijoy, V. Mishra, and M. N. Deo, "Development of in situ time-resolved Raman spectroscopy facility for dynamic shock loading in materials", *JINST* **12**, 11008 (2017). DOI: 10.1088/1748-0221/12/11/P11008
31. A. D. D. Chijioke, W. J. Nellis, A. Soldatov, and I. F. Silvera, "The ruby pressure standard to 150 GPa" *J. Appl. Phys.* **98**, 114905 (2005). DOI: https://doi.org/10.1063/1.2135877
32. HYADES is a commercial product of Cascade Applied Sciences email: larsen@casinc.com
33. SESAME: The Los Alamos National Laboratory Equation of state Database, 1995
34. E. R. Andrews, and R. G. Eades, "A nuclear magnetic resonance investigation of solid cyclohexane" *Proc. Royal Soc. A* **216**, 398 (1953). DOI: https://doi.org/10.1098/rspa.1953.0029
35. R. Kahn, R. Fourme, D. Andre, and M. Renaud, "Crystal structure of cyclohexane I and II" *Acta. Cryst.* **B29**, 131 (1973). DOI: https://doi.org/10.1107/S0567740873002074
36. N. B. Wilding, J. Carin, P.D. Hatton, and G. B. Wye, "Structural studies of cyclohexane IV" *Acta Cryst.* **B49**, 320 (1993). DOI: https://doi.org/10.1107/S0108768192007547
37. M. Pravica, Y. Shen, Z. Quine, E. Romano, and D. Hartnett, "High-Pressure Studies of Cyclohexane to 40 GPa", *J. Phys. Chem. B* **111**, 4103 (2007). DOI: https://doi.org/10.1021/jp070052b
38. X. Zheng, Y. Song, J. Zhao, D. Tan, Y. Yang, and C. Liu, "Nanosecond time-resolved Raman spectroscopy of molecular solids under laser-driven shock compression", *Chem. Phys. Lett.* **499**, 231 (2010). DOI: https://doi.org/10.1016/j.cplett.2010.09.058